CAD-based X-ray CT calibration and error compensation

Cédric Fragnaud, Clément Remacha, Julián Betancur, Stéphane Roux

CAD-based X-ray CT calibration and error compensation

Cédric FRAGNAUD[1,2], Clément REMACHA[2], Julián BETANCUR[2], and Stéphane ROUX[1]

[1] *Université Paris-Saclay, ENS Paris-Saclay, CentraleSupélec, CNRS, LMPS - Laboratoire de Mécanique Paris-Saclay, 91190, Gif-sur-Yvette, France*
[2] *Safran Tech, 78772 Magny les Hameaux, France*

February 1, 2022

Abstract

Artifacts due to imperfect determination of the scanner geometry, beam hardening and diffuse Compton scattering, limit the quantitative exploitation of radiographs or tomographies for non-destructive evaluation. Exploiting the CAD model of an industrial part, a methodology is proposed to refine the estimation of the CT-scanner geometry up to a scale factor, to correct or account for artifacts, and to assess the metrology of the part. A projective model describing the formation of X-ray images in CT-scanners is first introduced. The optimal parameters of the projective model are identified using a novel CAD-based calibration method that relies on the registration of simulated projections onto experimental ones. A metrological analysis based on the comparison between acquired and simulated X-ray images is proposed. A turbine blade, for which an automatic inspection procedure from few views is under development, is used as an example to illustrate the proposed methodology. The parametrization accounts for the refinement of the projection geometry, the calibration of beam hardening and the estimation of scattering. It is shown that, using the proposed procedure, the differences between acquired and simulated radiographic images are significantly reduced, indicating that the optimal parameters are properly identified. These differences are then exploited to detect flaws of the part.

Keywords – X-ray artifacts, Sensitivity fields, NDE

1 Introduction

After outstanding developments in medical applications [1, 2], X-ray Computed Tomography (CT) is rapidly being adopted for Non Destructive Evaluation (NDE) in industry [3, 4]. X-ray CT enables the verification of the integrity of industrial parts by, for instance, detecting porosities and cracks [5], verifying weaving patterns in 3D woven composites [6], and by performing dimensional metrology [3]. In particular, the detection of geometrical imperfections of turbine blades is of great importance in aeronautics to ensure the safety of passengers. Trained operators perform metrological analyses of turbine blades using radiographic imaging, usually either by examining a CT volume computed by a reconstruction algorithm [7, 8], or through the meticulous inspection of the images when insufficient projections are available. In this paper, an alternative approach is proposed: the comparison of projections acquired with a CT-scanner to projections simulated from the reference volume representing the ideal part, *i.e.* one without defects, allows the detection of geometrical imperfections of the inspected part.

Estimating accurate geometrical measurements is essential for an exhaustive detection of dimensional flaws. In these metrological applications, artifacts and time are limiting factors, especially in production where few projections are available.

Artifacts result from the deviation between the physical phenomena responsible for the formation of the image and the model used to describe it during the metrological analysis [9]. Indeed, the model is usually simplified as a geometrical projective model and with recourse to the Beer-Lambert's law to account for X-ray attenuation. Tomographic reconstruction methods or the raw analysis of X-ray images require an accurate determination of the projection geometry (*e.g.* source-to-object distance, projection angles). An inaccurate geometry definition undermines the quality of the reconstruction, *e.g.* generating blur

artifacts, and of the metrological analysis, *e.g.* from magnification effects. Tomographic reconstructions often rely on the strict application of Beer-Lambert's law, which is not perfectly obeyed in CT-scanners used for NDE. In this work, two main sources of errors are considered: beam hardening (BH) [10, 11] and Compton scattering [12, 13], both of which deteriorate X-ray image quality or fidelity.

The other limiting factor is time, which can be reduced but at the cost of increased noise. When using very noisy images, distinguishing noise from artifact-induced systematic deviations between measured and computed radiographs becomes increasingly difficult. Thus, a proper usage of fast scans calls for a very accurate determination of all artifacts.

Various techniques have been developed to mitigate X-ray CT artifacts.

- Projection geometry is usually determined via the study of the projections representing a calibration object whose geometry is known with a great accuracy [14, 15]. It can be further refined in software products when applying reconstruction algorithms to account for rotation axis offset. However, these steps may be insufficient to provide an accurate description of the tomograph set-up.

- The calibration of BH consists in acquiring radiographs of a known reference part and fitting a parametric function to the point cloud of pixelwise detector attenuation vs. traversed thickness by the least-squares method [10, 16]. This method produces satisfactory results but only a few parameters can be safely determined for the attenuation function.

- Signal processing techniques have been used to estimate scattered X-ray beams, *e.g.* by modeling the effect of scattered rays in pixel intensities as the convolution of the primary signal with a kernel to be identified [17, 18]. Deconvolution algorithms have also been proposed to obtain scatter-free projections, but their numerical stability is poor, leading to unreliable results [19, 20].

This paper proposes a CAD-based calibration method to estimate and correct projection geometry parameters, up to a scale factor, and artifacts in a unique formalism. It uses only the projection images of the inspected object and its numerical model (*e.g.* CAD model), *i.e.* does not require additional projection data, phantom object, or landmarks. The use of prior knowledge of the object shape and material yields an improvement in the quality of the estimation and the correction. Section 2 details the challenges addressed in this paper, namely the correction of the projection geometry, the calibration of BH and the estimation of scattering. Projection geometry parameters include the source-to-detector distance, the source rotation axis and the orientation of the imaged object. For BH, a parametric representation of the absorption length curve is used, which resumes the absorption calibration to the estimation of few parameters. Likewise, scattering is approximated by a convolution of the geometrical projection by a scattering kernel which is itself parametrized. In these three cases, it is proposed to formulate the problem as a parametric model, and fine tune those parameters so as to match observations. A description of the proposed methodology used to identify the optimal parameters for the model is given in section 3. Section 4 is devoted to the presentation of an example on which the CAD-based calibration procedure has been applied. It consists in the identification of the optimal parameters based on a reduced number of radiographic images of a turbine blade. The results are presented and discussed in Section 5.

2 Addressed problems

The intensity $I(\boldsymbol{x})$ measured at detector position $\boldsymbol{x} \in \Omega \subseteq \mathbb{R}^2$ is defined as the intensity of the incident X-ray beam attenuated along its path through the sample. The image $I_0(\boldsymbol{x})$ obtained when no sample lies between the source and the detector is called the flat-field image.

The attenuation image P, also called the projection, is derived from the intensity image I and the flat-field image I_0: $P = -\ln(I/I_0)$. Beer-Lambert law states that $P(\boldsymbol{x})$ is equal to the line integral of the material absorption coefficient along the line joining the source to the detector position $\boldsymbol{x}$. This relation is the main assumption used in all tomographic applications as it relates the measured data to the object geometry and composition. It is an excellent approximation for monochromatic and incoherent X-ray sources. However, scanner sources typically have a broad spectrum of energy, and hence Beer-Lambert's law is usually no more than an approximation.

The projection images are processed via reconstruction algorithms, image processing methods, or simulation of X-ray images, to get a better vision of the inspected part. Therefore, for computed tomography, numerical tools are of fundamental importance. The simulation of radiographic images is an easy linear

problem, but it makes use of an enormous amount of data. It is essential that such computations be very fast. One has the choice of commercial products or open-source tools. Commercial tools implement methods to simulate projections, taking into account multiple artifacts with elaborated physics-based models, however, they are not well fitted to the inverse problem analysis which is the purpose of reconstruction and of quantitative NDE. Open-source tools with high numerical efficiency, including GPU optimized codes (GPU-accelerated operations, optimized algorithms), are available [21], but are based on the unmodified Beer-Lambert's law. Such powerful open-source tools can still be used efficiently for optimizing image reconstructions if an accurate description of the formation of the images is established.

2.1 Projection geometry

The information on the projection geometry is usually determined before or after a tomographic acquisition, often using a calibration object with a well known geometry and which is easily readable from its projection [14, 22]. This step aims to deliver the geometrical description of the tomograph set-up captured in a set of parameters, *e.g.* position of source, axis of rotation (position and orientation), detector (position and orientation). However, these geometrical parameters may be inexact. The fine tuning of these parameters may be proposed to operators by the commercial reconstruction software based on a subjective assessment of the reconstruction quality which is useful because an inaccurate geometry description may compromise a proper reconstruction in particular for metrology assessment [23].

2.2 Beam Hardening

In CT systems, X-ray beams are polychromatic and the attenuation coefficient varies with photon energy, thus the simple Beer-Lambert attenuation law does not describe the absorption phenomenon well. Specifically the distribution of X-ray energies changes with the traveled distance in the material, and consequently the effective (*i.e.* integrating over all X-ray energies) absorption is no longer a material property. This phenomenon, known as beam hardening (BH), implies for a monomaterial, a non-linear relationship between the gray level of an attenuation image and the thickness of the part the beam passed through. Should Beer-Lambert's law still be used in the polychromatic case, a deviation between the model and the actual measurements would be observed. This would lead to a misinterpretation of the grayscale values where thicknesses are underestimated, yielding overestimated attenuation coefficients, which in turn deteriorates the quality of the reconstructed volume in the form of streaks and flares, known as beam hardening artifacts [11].

In the case of monomaterial parts, these artifacts can be corrected through the calibration of the attenuation. It consists in identifying the relationship between the gray level $P(\boldsymbol{x})$ of the measured attenuation image and the thickness of the material $T(\boldsymbol{x})$ the X-ray beam has gone through before hitting the pixel detector $\boldsymbol{x}$ (T is called a thickness map). It thus reduces to a non-linear gray level re-encoding represented by a function $U : \mathbb{R}^+ \mapsto \mathbb{R}^+$ such that $U(T(\boldsymbol{x})) = P(\boldsymbol{x})$, see Figure 1. A mere gray level re-encoding with U^{-1} allows an attenuation image P to be transformed into a thickness map T, hence enabling a legitimate use of Beer-Lambert's law even for polychromatic sources. The aim of BH correction is to determine the function u that best approximates U. Because it depends on the source technology and settings, u cannot be precomputed and is instead inferred from observations. The parameters of the correction function are usually identified by acquiring projections of a known reference part, then fitting the function to the point cloud — pixelwise detector attenuation vs. thickness — by the least-squares method [10, 16]. This fit is performed via the minimization of the error between observation and estimation, on a pixel-per-pixel basis. Such an approach does not allow for many parameters to describe the attenuation. Usually, odd order polynomials are chosen to keep the correction function monotonous, and a maximum polynomial order may be typically 5, leaving two unknown parameters [24, 25] since the linear term may be conventionally set to a unit prefactor. The proposed CAD-based calibration procedure permits many more degrees of freedom to be chosen while avoiding regression stability issues.

The function u is discretized over a basis of shape functions ϕ_k,

$$u(\xi) = \sum_{k=1}^{K} c_k \, \phi_k(\xi) \tag{1}$$

where c_k are parameters to be determined. u being defined up to an arbitrary scale factor, a convention is used to lift this degeneracy, for instance by imposing $\frac{\mathrm{d}u}{\mathrm{d}\xi} = 1$ for $\xi \sim 0$. A desirable property for ϕ_k

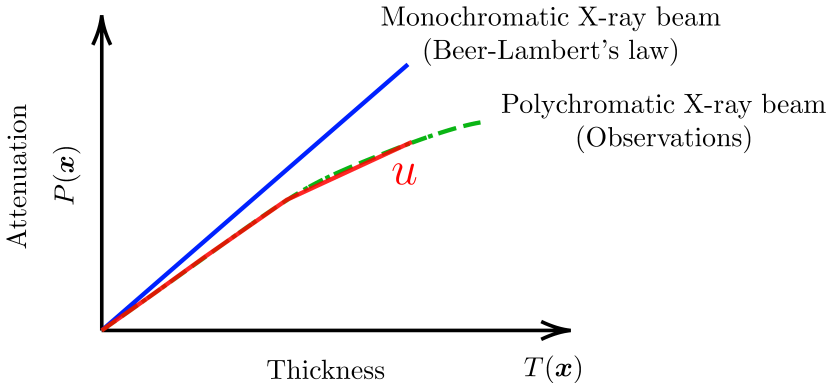

Figure 1: Differences between monochromatic assumptions (blue line), and polychromatic measurements (green dashed line). The aim is to determine the relationship between the two curves through the fit of a parametric function u (red line) to observed data.

is that the addition or removal of one of these functions has only a local effect on the function u. This amounts to saying that, for a given k, ϕ_k acts on a restricted range of values for ξ, *i.e.* ϕ_k has a compact support.

In this work, a piecewise-linear function for u is used. Besides its simplicity, it has the advantage of being a good interpolant of U with the property that, the more parameters, the better the interpolation, without loss of stability. Considering a discretization $\xi_0, \xi_1, \ldots, \xi_{K+1}$ of the gray levels of the thickness map, ϕ_k is the triangular function, compactly supported, defined by

$$\phi_k(\xi) = \begin{cases} \frac{\xi - \xi_{k-1}}{\xi_k - \xi_{k-1}} & \text{if } \xi_{k-1} \leq \xi < \xi_k \\ \frac{\xi_{k+1} - \xi}{\xi_{k+1} - \xi_k} & \text{if } \xi_k \leq \xi < \xi_{k+1} \\ 0 & \text{otherwise} \end{cases} \tag{2}$$

Once the function u described by (1) and (2) is identified, it can be applied to each pixel of the simulated projections. The study of the differences between acquired and simulated projections with the correction of BH assesses the relevance of this choice of model.

An optimal discretization must meet two conditions:

1. The discretization must properly reflect the curvature of the BH calibration function: the resolution of the mesh must be higher in zones of high curvature than in zones of low curvature,
2. The number of points observations covered by the shape function ϕ_k has to be large enough to estimate the corresponding parameter c_k.

To perform an ideal discretization satisfying condition 2., it is suggested to carry out a sampling via an arithmetic sequence on the cumulative frequency of the gray levels of T. This produces a sequence $\xi_0, \xi_1, \ldots, \xi_K$. The last shape function is extended to infinity assuming a constant value so that the model can cope with the highest material thicknesses: $\xi_{K+1} = +\text{“}\infty\text{”}$ (in practice, a sufficiently high value, *i.e.* maximum thickness, is chosen). This discretization can be further refined so that condition 1. is verified, potentially at the expense of increasing the number of interpolation shape functions and thus the number of parameters.

2.3 Compton scattering

In a radiographic image, over-intensities are observed in regions away from the part where the absorption of X-rays is null or negligible. They originate from X-rays scattered away by the sample due to, inter alia, the Compton effect (Figure 2).

The measured intensity at pixel $\boldsymbol{x}$ is described as the sum of two components: a primary one $I_P(\boldsymbol{x})$, derived from photons passing directly through the object without scattering or absorption, and a secondary contribution $I_S(\boldsymbol{x})$, that corresponds to photons scattered away from the initial trajectory by the Compton effect. Although scattering leads to complications in the analysis of radiographic images, it has a very minor effect in most applications of material science where energies are large (in contrast

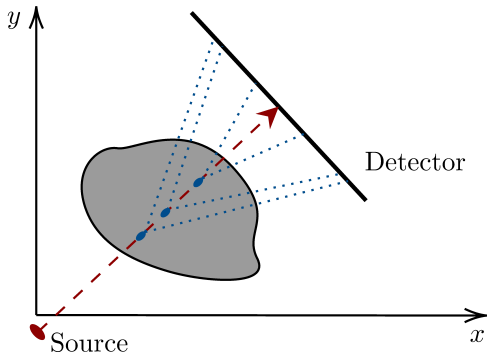

Figure 2: Illustration of Compton effect. A beam emerging from the source interacts along its path with the atoms of the object: X-ray photons are scattered away from their initial trajectory, leading to an additional signal captured by the detector.

to medical applications). Hence scattering is treated as a small perturbation and multiple scattering is neglected in front of single scattering. Usually, CT reconstruction does not account for scatter, leading to artifacts in the reconstructed volume such as streaking or cupping [11, 13]. It may also cause a deviation of dimensional measurements from their actual values because of the difficulty to position edges precisely.

Methods using signal processing techniques have been developed to estimate and correct for scattering effects. The scattered X-ray distribution can be predicted via Monte-Carlo (MC) simulations [26, 27]. Although it is a powerful tool, the poor convergence properties of MC sampling leads to time consuming calculations. Point-Spread Functions (PSFs) have been used to describe single scattering of the pencil beam [28, 29, 30, 31]. PSFs are represented as the convolution between the incident photon flux and a kernel to be determined.

The above modelling is 3D and thus costly and difficult to be coupled to tomographic reconstruction. Following [18, 19, 20], it is proposed to resort to an approximation that captures a large part of the scattering. The approximation formulas are derived from an expression of the scattered intensity based on the interactions a beam undergoes as it propagates through the object [32]. The intensity $I_S(\boldsymbol{x})$ received at a pixel $\boldsymbol{x}$ from all the scattered rays is expressed as

$$I_S(\boldsymbol{x}) = \int_{\boldsymbol{x'}} T(\boldsymbol{x'})\, I_0(\boldsymbol{x'})\, e^{-T(\boldsymbol{x'})/\xi}\, G(\boldsymbol{x'} - \boldsymbol{x})\, \mathrm{d}\boldsymbol{x'} \tag{3}$$

where T is the thickness map, I_0 is the flat-field image, ξ is the attenuation length of the radiation, and G is a scatter kernel to be estimated. As long as the scattering occurs in a short range ($\boldsymbol{x'} - \boldsymbol{x}$ small as compared to ξ), the gradient of I_0 may be ignored so that $I_0(\boldsymbol{x'})/I_0(\boldsymbol{x}) \approx 1$, and thus

$$I_S(\boldsymbol{x})/I_0(\boldsymbol{x}) = (I_A * G)\,(\boldsymbol{x}) \tag{4}$$

with $I_A(\boldsymbol{x}) = T(\boldsymbol{x})\, e^{-T(\boldsymbol{x})/\xi}$.

The kernel G is parametrized, *i.e.* represented as the weighted sum of basic kernels k_σ,

$$G(\boldsymbol{x}) = \sum_{\sigma \in \Sigma} a_\sigma\, k_\sigma(\boldsymbol{x}) \tag{5}$$

with $\Sigma \subset \mathbb{R}^+$. Coefficients a_σ need to be adjusted to the best fit of the observations. The parametrization is expected to account for the effective scatter distribution with a reasonable number of parameters. The contribution of Compton scattering suggests that the kernel is bell-shaped. A superposition of Gaussian functions can be chosen to describe it, so that the kernels k_σ are modeled as

$$k_\sigma(\boldsymbol{x}) = g_\sigma(\boldsymbol{x}) - \frac{\delta(\boldsymbol{x})}{2\pi\sigma^2} \tag{6}$$

where g_σ is the 2D-Gaussian filter with standard deviation σ. The introduction of the Dirac function δ is based on the observation that photons that were supposed to reach the detector at pixel $\boldsymbol{x}$, but that have been deflected, reach the detector at another pixel. Hence, its contribution is removed from the

measured signal. This part of the kernel is merely equivalent to increasing the absorption in proportion to the crossed thickness $T(\boldsymbol{x})$, as if the coefficient of absorption of the material were slightly increased by the total amount of scattering. Note that the beam may also be scattered away from the detector, and here again contributes to an additional attenuation. In the end, provided that an adjustment of the attenuation coefficient is considered (as for BH correction), δ in (6) may be omitted.

In order to account for scattered photons that reach the detector over a broad range of distances from pixel $\boldsymbol{x}$, the set $\Sigma = \left\{2^k, k \in \mathcal{L} \subset \mathbb{R}^+\right\}$ is suggested. This geometric progression is introduced to limit the overlap of Gaussian kernels g_σ which would render the determination of the kernel ill-conditioned.

Once the kernel G is identified, the correction of the images produced by the system via deconvolution techniques should be avoided because it is known to be an ill-behaved problem generating spurious high frequency signals. Instead, an alternative method consists in computing the scatter signal by numerically simulating the radiographic images and by convolving them with the kernel G. The subtraction of this signal from the acquired images is expected to produce close to scatter-free radiographic images provided they are properly registered.

The correction of the above artifacts as well as the determination of the precise geometry of the tomograph finally reduce to a single problem: the identification of the optimal parameters needed to produce an accurate synthetic radiographic image from a known object geometry and a numerical simulation of the projection.

3 Calibration of parameters

A calibration procedure, based on sensitivity fields, is proposed to identify optimal parameters for the model describing the formation of images in X-Ray CT-scanners. This model is defined by the projection geometry parameters $\boldsymbol{p} = (p_k)$, the coefficients $\boldsymbol{c} = (c_k)$ of the beam hardening calibration function (1), and the amplitudes $\boldsymbol{a} = (a_\sigma)$ of the scattering kernel (6).

Suppose the K parameters d_k, gathered in a vector $\boldsymbol{d} = (d_k)$, are to be identified. Let $P_{\mathrm{a}}^n(\boldsymbol{x})$, $n \leq N$, be the N projections acquired with a CT-scanner, regarded as reference images. Given an initial estimate $\boldsymbol{d^0}$ and a reference volume of the inspected part, projections $P_{\mathrm{s}}^n(\boldsymbol{x}; \boldsymbol{d^0})$ are numerically simulated. The reference volume representing the ideal design can have several formats: a CAD model described by analytical functions or by a polygon mesh, a tomographic volume, *etc.* The sensitivity fields

$$s_k^n(\boldsymbol{x}) = \left.\frac{\partial P_{\mathrm{s}}^n(\boldsymbol{x}; \boldsymbol{d})}{\partial d_k}\right|_{\boldsymbol{d}=\boldsymbol{d^0}} \tag{7}$$

are then computed. The partial derivatives involved in the calculation of these fields may be approximated by finite differences

$$s_k^n(\boldsymbol{x}) = \frac{P_{\mathrm{s}}^n\left(\boldsymbol{x}; \boldsymbol{d^0} + h\,\boldsymbol{e}_k\right) - P_{\mathrm{s}}^n\left(\boldsymbol{x}; \boldsymbol{d^0}\right)}{h} \tag{8}$$

where $\boldsymbol{e}_k$ refers to the k^{th} vector of the canonical basis of the space of parameters, *i.e.* $(\boldsymbol{e}_k)_i = \delta_{ki}$. These sensitivity fields quantify how small perturbations around the value $\boldsymbol{d^0}$ affect the simulated projections $P_{\mathrm{s}}^n(\boldsymbol{x})$ for each parameter d_k.

Projection residuals $\rho_{\boldsymbol{d^0}}^n(\boldsymbol{x}) = P_{\mathrm{a}}^n(\boldsymbol{x}) - P_{\mathrm{s}}^n(\boldsymbol{x}; \boldsymbol{d^0})$, *i.e.* the differences between X-ray acquisitions and simulated projections, are interpreted as resulting from the misidentification of the parameters. In order to quantify the discrepancy between estimated and optimal parameters, these residuals are projected in the least-squares sense onto the sensitivity vectors,

$$\boldsymbol{\delta d}^* = \arg\min_{\boldsymbol{\delta d}} \sum_{n=1}^{N} \left\|\rho_{\boldsymbol{d^0}}^n(\boldsymbol{x}) - \boldsymbol{s^n}(\boldsymbol{x})\ \boldsymbol{\delta d}\right\|_2^2 \tag{9}$$

where the notation $\boldsymbol{s^n}(\boldsymbol{x}) = \begin{pmatrix} s_1^n(\boldsymbol{x}) & \dots & s_K^n(\boldsymbol{x}) \end{pmatrix}$ is used, and $\boldsymbol{\delta d}$ is the column vector containing the variables of the minimization problem. The use of the L_2-norm can be justified as being optimal when the images $P_a^n(\boldsymbol{x})$ are polluted by white Gaussian noise: the maximum of the log-likelihood corresponds to the minimum of the L_2-norm. Assuming a Poisson noise on $I(\boldsymbol{x})$ and $I_0(\boldsymbol{x})$, a change in the expression of (9) into a weighted sum may be used to take into account the local uncertainty. $\boldsymbol{\delta d}^*$ represents the error

made in the identification of the parameters, and thus provides the amount by which the parameters $\boldsymbol{d^0}$ are to be changed to reduce the discrepancy between $P_{\mathrm{a}}^n(\boldsymbol{x})$ and $P_{\mathrm{s}}^n(\boldsymbol{x};\boldsymbol{d^0})$. This value is given by

$$\boldsymbol{\delta d}^* = \boldsymbol{H}^{-1}\boldsymbol{b} \tag{10}$$

where the matrix $\boldsymbol{H}$ is defined by

$$H_{ij} = \sum_n \sum_{\boldsymbol{x}} s_i^n(\boldsymbol{x})\, s_j^n(\boldsymbol{x})\, w^n(\boldsymbol{x}) \tag{11}$$

and $\boldsymbol{b}$ is the vector whose components b_k are given by

$$b_k = \sum_n \sum_{\boldsymbol{x}} s_k^n(\boldsymbol{x})\, \rho_{\boldsymbol{d}^0}^n(\boldsymbol{x})\, w^n(\boldsymbol{x}) \tag{12}$$

with $w^n(\boldsymbol{x})$ the reciprocal of the variance of the noise polluting $P_a^n(\boldsymbol{x})$. Note that $\boldsymbol{H}$ represents the matrix of the second derivatives of the cost function (9) with respect to $\boldsymbol{\delta d}$, assuming the sensitivity fields $s_k^n(\boldsymbol{x})$ do not depend on $\boldsymbol{\delta d}$, and is thus referred to as the Hessian matrix.

Repeating this CAD-based calibration procedure usually leads to a fixed point solution (one that no longer evolves) after few iterations. Although there is no guarantee to obtain a unique solution, the proposed parametrization together with the use of a complex shape CAD model (with high and low frequency power) and a good initialization make the problem well behaved.

It is important to emphasize that if the observed object differs from its model by a mere homothety, the projection geometry parameters can be adjusted to inexact values and yet produce a perfect match of the projections. Assuming the analyzed object has a complex shape, this scale factor is the only degeneracy of the geometrical calibration. It can only be lifted if one additional length measurement is performed and used jointly in the calibration process.

It should be noted that the very same procedure holds for any set or subset of parameters. Because of non-linearities, the order in which subsets may be considered is important. An appropriate rule is to rank the impact of the projection geometry, beam hardening and Compton scattering, and fit corresponding parameters in descending impact order. The impact can be assessed by the observation of the projection residuals computed before any correction.

4 Case study

The inspection of a turbine blade (Figure 3) was selected as a case study to illustrate this methodology. This mono-material part is made of a monocrystalline nickel alloy.

Figure 3: View of a turbine blade [33].

The reference volume representing the ideal part was the CAD model of the part described by a polygon mesh. To obtain a universal structure — *i.e.* usable by a vast majority of software — describing the 3D volume, it was discretized into voxels whose size were 0.05 mm using a ray tracing algorithm similar to that described in [34]. Each voxel was characterized by a binary numerical value (0 or 1) depending on whether it lies inside or outside the object.

A set of $N = 6$ intensity images representing the turbine blade from complementary points of view were exploited, each image being obtained from the average of 2 frames with an exposure time of 354 ms each. This is in line with the number of views routinely used for their inspection. The images have been acquired with the XT H 450 system developed by Nikon Metrology, with a high-energetic source of 390kV. The tube current was set to 641 μA. The system produced 2000 $\times$ 2000-pixel radiographs, each pixel being encoded as a 16-bit unsigned integer. The associated attenuation images were denoted $P_{\mathrm{a}}^n, n \leq N$.

From the reference volume, attenuation images $P_{\mathrm{s}}^n, n \leq N$, were simulated using the ASTRA Toolbox [21]. The latter proposes projection operators with highly flexible source/detector positioning, GPU-acceleration and is callable from Matlab and Python. A scale factor for the gray levels of the reference volume has been adjusted (by taking into account the actual attenuation coefficient of the part) so that the projection P_{s}^n of the binarized volume matches the true projection P_{a}^n.

The following description of the parameters was used to perform the calibration.

- The projection geometry was controlled by a vector $\boldsymbol{p}$ of 14 parameters: the size of detector pixels, the source-to-object distance (SOD), the 6 components of the position of the detector (3 translations, one of which with respect to the source via the source-to-detector distance, SDD, and 3 rotations), and the 6 components of the position of the studied object (3 rotations and 3 translations).

- The BH calibration function u was modeled as a sum of $K = 8$ triangular functions ϕ_k controlled by a K-component vector $\boldsymbol{c}$. In the simulated images, the attenuation of the X-ray beam follows the Beer-Lambert's law, so that $P_s^n(\boldsymbol{x}) \propto T^n(\boldsymbol{x})$ where T^n denotes the n^{th} thickness map. This relation is based on the assumption that the simulated images perfectly match the acquired images. Although it may not be actually the case at the beginning of the CAD-based calibration procedure, it becomes more and more valid along iterations. Hence, the discretization described in Section 2.2 was performed, not on the gray levels of the unknown T^n, but on those of P_{s}^n. The last discretization point was set to $\xi_{k+1} = 20$.

- Regarding the scatter kernel used to reproduce the scatter signals and described by a vector $\boldsymbol{a}$ of 7 parameters, the gaussian standard deviations σ are defined by the sequence $\Sigma = \left\{2^k, 2 \leq k \leq 8\right\}$.

The CAD-based calibration procedure was performed using restricted (rectangular) Regions Of Interest (ROIs) of the images. The information on the projection geometry and BH only come from the region containing the projection of the object. On the other hand, the scatter is more observable in regions outside of it (as it is clearly due only to scattering, and does not depend on the other parameters such as geometry or BH), more specifically next to regions containing the projection of the thickest part of the object. Based on these elements, two ROIs were considered for each view, as illustrated in Figure 4, depending on which parameters were being fine-tuned. If only a subset of images is considered, the procedure is not optimal but is much faster (less data to process), and the benefit of using all data is modest provided the subregions are well chosen.

The calibration of the parameters $\boldsymbol{p}$, $\boldsymbol{c}$ and $\boldsymbol{a}$ was conducted iteratively according to the procedure described in Algorithm 1. A misregistration between observed and simulated images is likely to be confused with small angle scattering, distorting the entire calibration procedure. Hence, the scatter parameters were at first not considered, and were added to the procedure after the parameters $\boldsymbol{p}$ and $\boldsymbol{c}$ first converge. The first and final convergence criteria can be based on a maximum number of iterations, on the computed increments ($\boldsymbol{\delta p}^*$, $\boldsymbol{\delta c}^*$ and $\boldsymbol{\delta a}^*$), or, as used in this work, on the discrepancies between observed and simulated projections after the iteration. The order in which the calibrations were performed was based on the above-mentioned principle. Close to the fixed point, one may refine the parameters in any order.

A study has been performed to quantify the noise polluting a projection and thus determine $w^n(\boldsymbol{x})$. A series of intensity images representing the turbine blade from the same point of view have been acquired without modifying the acquisition parameters. The cologarithm of these images normalized by the flat-field image are computed. A mean projection, *i.e.* noiseless, is determined, which allows the extraction of the noise polluting the projections. Its variance is given by $V(\boldsymbol{x}) = \sigma^2 \left(\frac{1}{N(\boldsymbol{x})} + \frac{1}{M(\boldsymbol{x})}\right)$, with $\sigma^2 \approx 1.7 \times 10^{-5}$ (for the CT-scanner and acquisition parameters used), and where $N(\boldsymbol{x})$ and $M(\boldsymbol{x})$ correspond to the noiseless (*i.e.* simulated) intensity image and flat-field image, respectively.

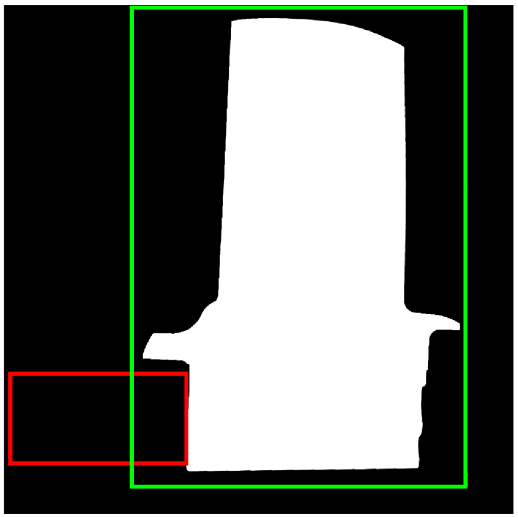

Figure 4: Example of the two ROIs for one view. The ROI associated to the calibration of the projection geometry and BH is displayed in green, the one associated to the calibration of scattering is displayed in red.

Algorithm 1: Iterative calibration procedure

Data: Initial estimations $\boldsymbol{p}^{\mathbf{0}}$, $\boldsymbol{c}^{\mathbf{0}}$, $\boldsymbol{a}^{\mathbf{0}}$
Result: Optimal values $\boldsymbol{p}^{*}$, $\boldsymbol{c}^{*}$, $\boldsymbol{a}^{*}$
do
  Simulate images with the current parameters $\boldsymbol{p}$, $\boldsymbol{c}$ and $\boldsymbol{a}$;
  Compute $\boldsymbol{\delta p}^{*}$ using (10) and update $\boldsymbol{p} \leftarrow \boldsymbol{p} + \boldsymbol{\delta p}^{*}$;
  Simulate images with the current parameters $\boldsymbol{p}$, $\boldsymbol{c}$ and $\boldsymbol{a}$;
  Compute $\boldsymbol{\delta c}^{*}$ using(10) and update $\boldsymbol{c} \leftarrow \boldsymbol{c} + \boldsymbol{\delta c}^{*}$;
  if *First convergence criterion reached* **then**
    Simulate images with the current parameters $\boldsymbol{p}$, $\boldsymbol{c}$ and $\boldsymbol{a}$;
    Compute $\boldsymbol{\delta a}^{*}$ using (10) and update $\boldsymbol{a} \leftarrow \boldsymbol{a} + \boldsymbol{\delta a}^{*}$;
while *Final convergence criterion reached*;

Once the parameters estimated, the BH and scatter are reproduced on the simulated images, which are then denoted with a star superscript, $P_s^{n,*}$.

5 Results and discussions

The discrepancy between a simulated and acquired intensity image before and after the CAD-based calibration procedures for restricted regions of interest of the image is displayed in Figure 5. Prior to any adjustments, the differences were mostly due to an incorrect projection geometry, whose correction is illustrated in Figure 6. The major change concerns the adjustment of the position and orientation of the volume, and of the position of the detector, see Table 1. The second most important factor was the correction of gray levels brought by BH corrections. The reproduction of BH lead to an attenuation of the differences inside the part, thus allowing a better interpretation of the graylevel intensities as the thickness of material crossed by the beam. By reproducing scattering, the differences around the part were reduced, resulting in a finer edge definition. Figure 5 shows that the mis-estimation of the projection geometry and the beam hardening phenomena have a greater impact than the scatter (most visible in subfigures c and d). This observation confirms the order chosen in Algorithm 1. Figure 7 indicates that a stable solution was reached after only a few iterations. The norms of residuals were reduced on average from 959 to 96, that is by a factor of 10.

It is assumed that, after the CAD-based calibration procedure, $P_s^{n,*}$ perfectly matches P_a^n, $\forall n$. Let $P_s^{n,+}$ be the simulated attenuation images after the calibration procedure, but for which the BH is left

Parameter	Initial estimation	Final estimation	Change
Size of detector pixels (mm)	0.20	0.21	0.01
SOD (mm)	226.43	217.96	-8.47
SDD (mm)	1009.67	1034.67	24.99
Translation vector of the detector (mm)	0.00 0.00	-2.60 13.64	-2.60 13.64
Rotation angles of the detector (deg)	0.00 0.00 0.00	-0.16 -0.18 -0.15	-0.16 -0.18 -0.15
Translation vector of the studied object (mm)	3.14 8.97 0.45	5.99 17.20 4.26	2.85 8.23 3.81
Rotation angles of the studied object (deg)	0.00 0.00 0.00	-3.30 2.07 1.03	-3.30 2.07 1.03

Table 1: Change in the projection geometry.

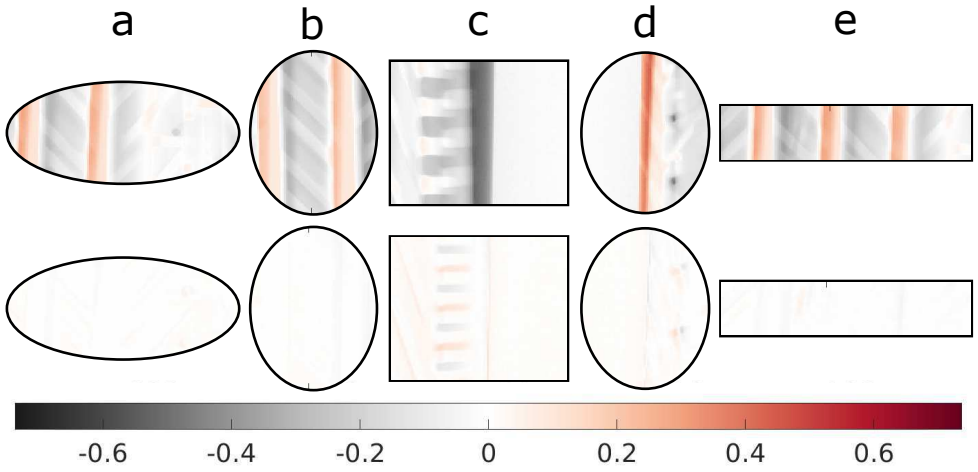

Figure 5: Difference (color) between acquired and simulated intensity images, before (top) and after (bottom) identification of the projection geometry and consideration of BH and scatter artifacts.

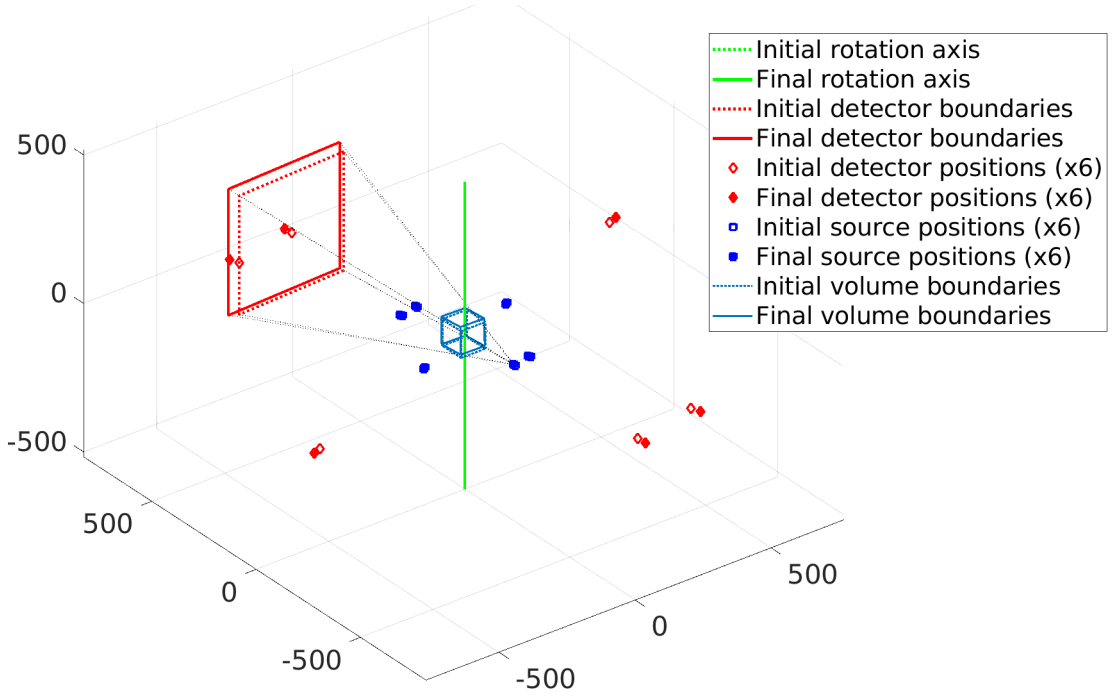

Figure 6: Modification of the projection geometry using the proposed CAD-based calibration method for $N = 6$ (distance expressed in mm).

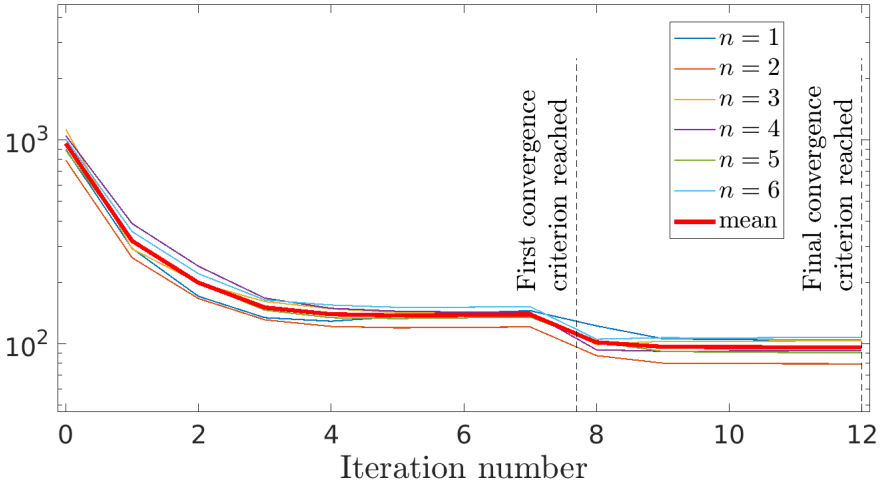

Figure 7: Evolution of the L_2-norm of residuals over iterations.

uncorrected. As stated before, the simulation of radiographic images is based on the Beer-Lambert's law, so that $P_s^{n,+}(\boldsymbol{x}) \propto T^n(\boldsymbol{x})$. Thus, by generating the point cloud $(P_s^{n,+}, P_a^n)$ one can observe the discrepancy between the Beer-Lambert's law and the experimental measurements, see Figure 8(a). The estimated function u provides a good approximation of the scatter plot of the projection data P_a^n. It is shown that a different discretization, from 4 to 12 parameters (Figure 8(b)), leads to a similar function. By applying u to each pixel of $P_s^{n,+}$, the simulated images $P_s^{n,*}$ were more faithful to reality, as shown by the residuals Figure 5.

This quality of calibration can be explained by the fact that, unlike the usual approaches, the spatial correlations of the projection were exploited. The measured image resulted from the projection of a part on the detector. This part provided information on the expected gray levels given its geometry, position and orientation in space and chemical composition. The proposed methodology used this knowledge to produce a more stable and accurate calibration of BH.

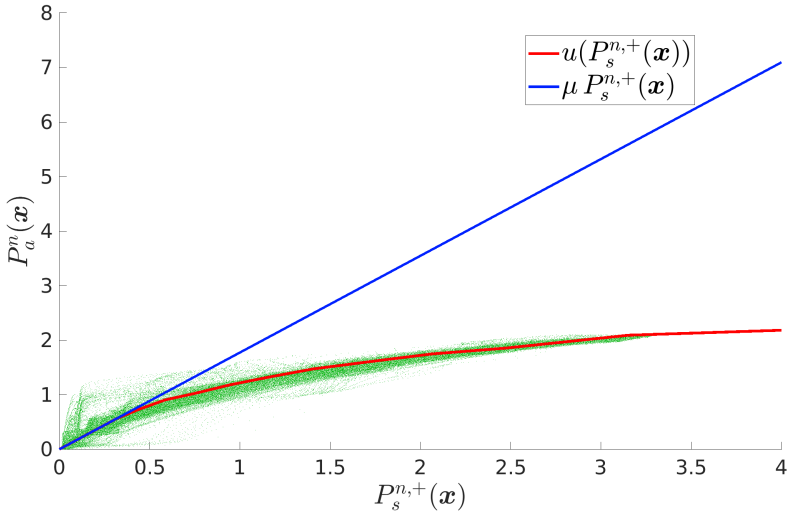

(a)

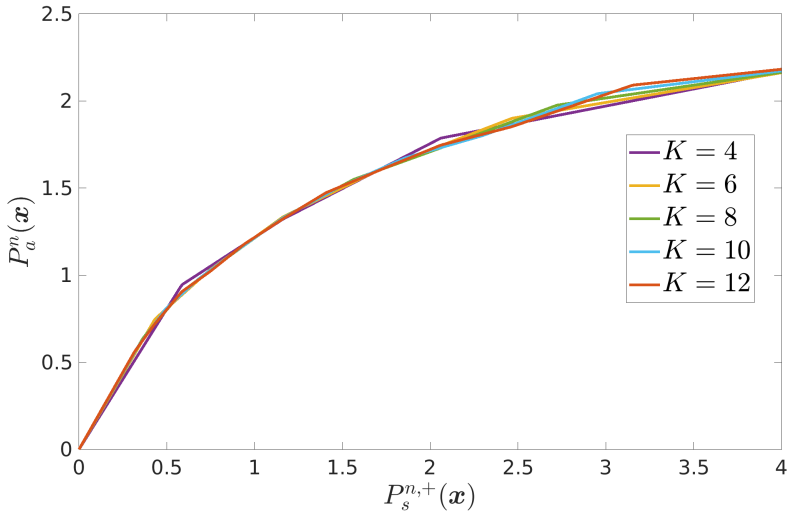

(b)

Figure 8: Result of the calibration of BH. (a) Result for a view n restricted to the associated ROI with K=8. The blue line shows the ideal case given by Beer-Lambert's law, *i.e.* no beam hardening. The green point cloud presents the measurement $P_a^n(\boldsymbol{x})$. The red curve shows the piece-wise linear function u after calibration of the parameters c_k. (b) Estimated piece-wise linear function u with less and more parameters.

The estimated scatter kernel G is represented in Figure 9. At high energy, the scattering probabilities

are rather small, and a photon is mostly scattered in the forward direction. Then, the intensity of the scatter signal is negligible as compared to that of the primary signal. These characteristics were observed here as the scatter kernel has a low amplitude and a small radius. In CT, the correction of such a signal is not necessary, but it becomes crucial when individual radiographs are to be quantitatively analyzed.

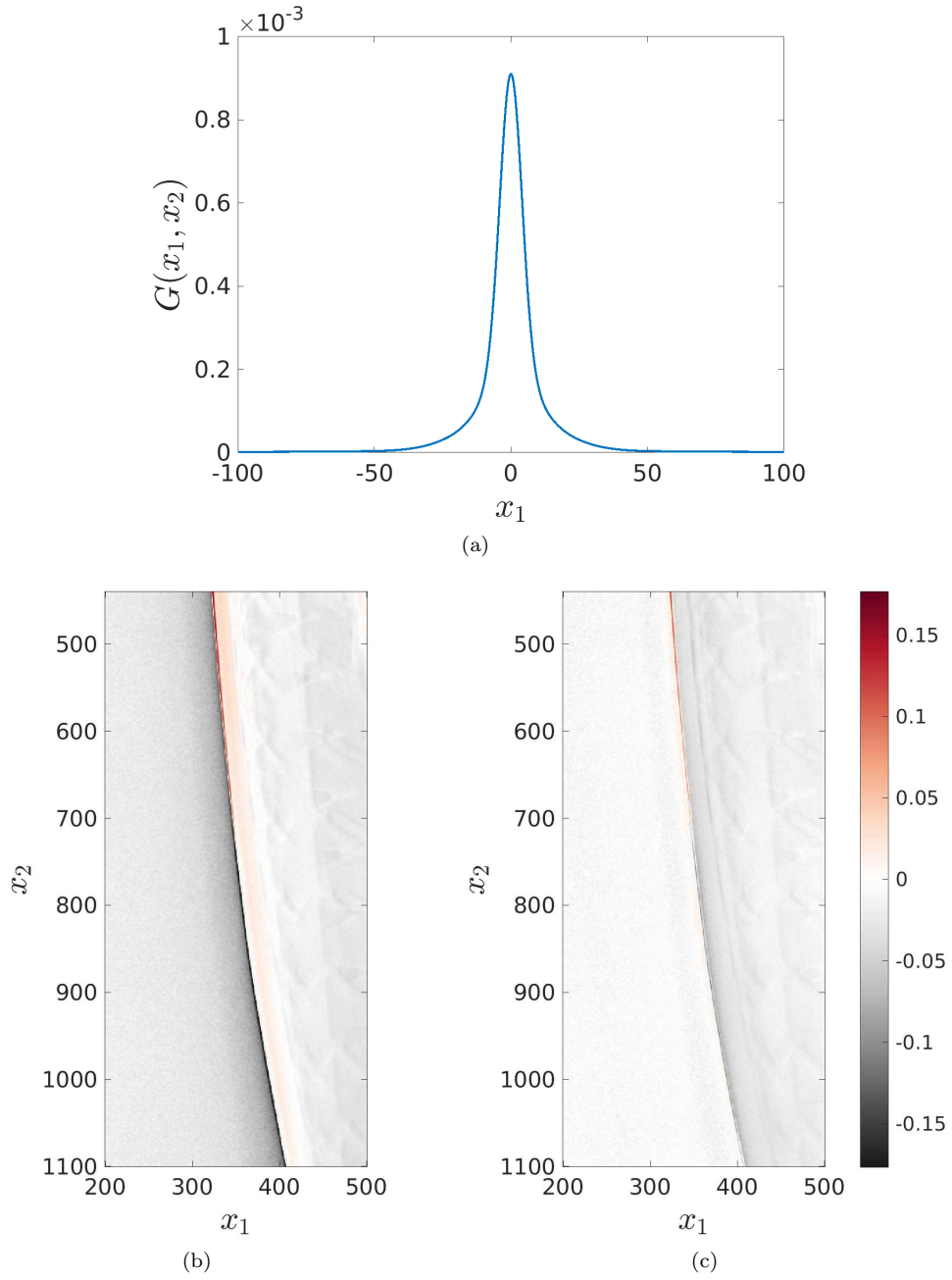

Figure 9: (a) Estimated scatter kernel G over x_1 for $x_2 = 0$. Difference (color) between acquired and simulated intensity images (b) without and (c) with scatter correction.

The final differences, Figure 5 bottom, represent the deviation between the ideal part (CAD model) and the inspected part. A small difference in thickness at the trailing edge of the blade (subfigure c) is observed, and two cooling holes (subfigure d) are misplaced. These two differences have no consequence on the quality of the produced part, but simply reveals the excellent sensitivity of the analysis after proper calibration. They would not be detectable from the raw data (Figure 5 top).

The identified parameters are used to enhance the quality of the tomographic volume. A set of 3000 projections have been acquired using the same CT-scanner and acquisition parameters than the

few projections exploited to estimate the optimal parameters. The associated tomographic volume is calculated (i) without any gray level correction on the projections and (ii) after using the function u^{-1} on the gray levels of the projections. Two regions of slices of the reconstructed volume are displayed in Figure 10. They indicate that the gray level gradients in homogeneous area are highly reduced, while being increased at the frontiers between the part and the background. This phenomena is observed at a global scale (exterior surface, see Figures 10a and 10c) and at a more local scale (cooling holes, see Figures 10b and 10d). During the industrial inspection process, the tomographic volume is segmented into two parts: the object and the background. The volume reconstructed using corrected projections would lead to a more faithful segmentation and thus a more accurate control.

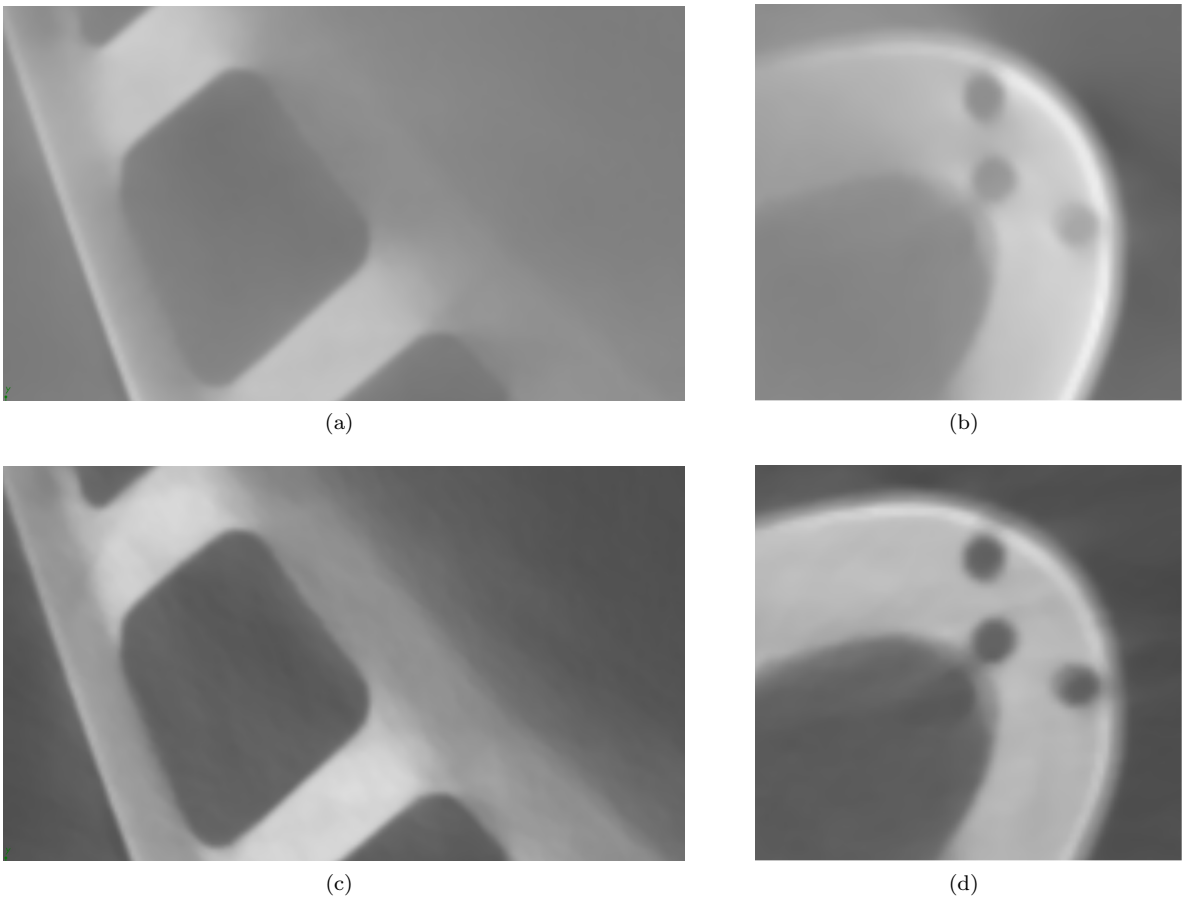

(a) (b)

(c) (d)

Figure 10: Tomographic volumes using (a) and (b) uncorrected projections, (c) and (d) projections corrected with the identified function u^{-1}.

The findings of this study does have some limitations. Some phenomena that result in artifacts, *e.g.* afterglow, are still to be included in the model. The proposed method renders such additional corrections easily accessible once a suitable parametrization is formulated. Regarding the identification of the projection geometry, the use of a simple geometry part might lead to an ill-posed problem. This point was not addressed nor studied in this work. Additionally, the sensitivity fields rely on a linearization of the problem, which suggests that only small corrections are accessible to the procedure. This can be relaxed by a coarse-grained (*i.e.* multi-scale) procedure, in which the residuals and sensitivity fields are observed at the most relevant scale. Finally, in practice, another limitation is the important computation time due to the voxelisation step. The voxelisation algorithm may be improved (*e.g.* parallelized) to make this step faster. Other strategies can be adopted to improve the execution time, *e.g.* compute the sensitivity fields in a single judiciously chosen direction and deduce the sensitivity fields in the other directions from the ones of the previous iteration. This limits the number of voxelisation steps by iteration. Other X-ray simulation tools that uses directly the CAD model, and thus does not require a voxelisation step, might reduce the computation time.

6 Conclusion

A parametric model describing the formation of images in X-ray CT-scanners that embeds phenomena occurring during acquisition, namely the Compton scattering and beam hardening, is presented. A calibration procedure is proposed to estimate the optimal values of the model parameters. Using the differences between observations and numerical simulations from the CAD model, their norm is minimized through the use of sensitivity fields. This method requires the acquisition of a few projections, without any calibration object, phantom or landmark. Applied to a case study, the associated iterative algorithm has shown the feasibility and interest of the method as the residuals were significantly attenuated throughout the procedure. Only a few iterations are needed to obtain a stable solution with a reduced number of views. The CAD-based calibration procedure introduced in this paper allowed the determination of the projection geometry and estimate X-ray artifacts arising from different phenomena.

The chosen parametrization ensures a well-behaved problem. The geometric correction however suffers from a degeneracy issue involving a scale factor, which is easily lifted by one additional length measurement. The number of parameters appears to have no impact on the quality of the calibration, provided that no degeneracy of the parametrization is introduced. The multi-view nature of the procedure is essential to produce a good estimate as it permits the model to take full advantage of different angles of projection.

In this study, the procedure has been carried out with a reduced number of views to meet the industrial demand for Non Destructive Evaluation of turbine blades. The final residuals reveal the discrepancies between the inspected part and the ideal design given by the CAD model. Based on this analysis, a NDE can be performed to control the part under inspection. For instance, a baseline measurement, *e.g.* derived from the noise found in a radiographic image, allows the detection of dimensional irregularities. It is shown that the estimated artifact corrections enhance the quality and reliability of the reconstructed tomographic volumes.

The question of the number of projections to be exploited is interesting. The method requires a minimal amount of information to estimate the various parameters. As more images N are considered, the accuracy of the parameters is expected to be increased, but more and more faintly with N whereas the processing time increases essentially linearly with N.

Acknowledgement

This work was supported by the French “Association Nationale de la Recherche et de la Technologie” (CIFRE n°2019/0793). The authors would like to thank Ms. Tonya Rose from the Digital Sciences and Technologies Departement at Safran for constructive feedback of the manuscript.

References

[1] Willi A. Kalender. *Computed tomography: fundamentals, system technology, image quality, applications*. John Wiley & Sons, 2011.

[2] Benjamin Pooya Fahimian, Yunzhe Zhao, Zhifeng Huang, Russell Fung, Yu Mao, Chun Zhu, Maryam Khatonabadi, John J. DeMarco, Stanley Joel Osher, Michael F. McNitt-Gray, and Jianwei Miao. Radiation dose reduction in medical x-ray CT via Fourier-based iterative reconstruction. *Medical Physics*, 40(3):031914, 2013.

[3] Jean-Pierre Kruth, Markus Bartscher, Simone Carmignato, Robert Schmitt, Leonardo De Chiffre, and Albert Weckenmann. Computed tomography for dimensional metrology. *CIRP Annals*, 60(2):821–842, 2011.

[4] Thomas De Schryver, Jelle Dhaene, Manuel Dierick, Matthieu N. Boone, Eline Janssens, Jan Sijbers, Mattias van Dael, Pieter Verboven, Bart Nicolai, and Luc Van Hoorebeke. In-line NDT with X-Ray CT combining sample rotation and translation. *NDT & E International*, 84:89–98, 2016.

[5] Petr Hermanek and Simone Carmignato. Porosity measurements by X-ray computed tomography: Accuracy evaluation using a calibrated object. *Precision Engineering*, 49:377–387, 2017.

[6] Arturo Mendoza, Julien Schneider, Estelle Parra-Denis, and Stéphane Roux. Measuring yarn deformations induced by the manufacturing process of woven composites. *Composites Part A: Applied Science and Manufacturing*, 120:127–139, 2019.

[7] Lee A. Feldkamp, L. C. Davis, and James W. Kress. Practical cone-beam algorithm. *Journal of the Optical Society of America A*, 1(6):612–619, 1984.

[8] Marcel Beister, Daniel Kolditz, and Willi A. Kalender. Iterative reconstruction methods in X-ray CT. *Physica Medica*, 28(2):94–108, 2012.

[9] Thorsten Buzug. *Computed Tomography : From Photon Statistics to Modern Cone-Beam CT*. Springer, 2008.

[10] Rodney A. Brooks and Giovanni Di Chiro. Beam hardening in X-ray reconstructive tomography. *Physics in Medicine & Biology*, 21(3):390–398, 1976.

[11] Bruno De Man, Johan Nuyts, Patrick Dupont, Guy Marchal, and Paul Suetens. Metal streak artifacts in X-ray computed tomography: a simulation study. In *1998 IEEE Nuclear Science Symposium Conference Record. 1998 IEEE Nuclear Science Symposium and Medical Imaging Conference (Cat. No. 98CH36255)*, volume 3, pages 1860–1865. IEEE, 1998.

[12] Avinash C. Kak, Malcolm Slaney, and Ge Wang. Principles of computerized tomographic imaging. *Medical Physics*, 29(1):107, 2002.

[13] Ralf Schulze, Ulrich Heil, Daniel Gross, Dan Dominik Bruellmann, Egor Dranischnikow, Ulrich Schwanecke, and Elmar Schoemer. Artefacts in CBCT: a review. *Dentomaxillofacial Radiology*, 40(5):265–273, 2011.

[14] Pavel Müller. *Coordinate Metrology by Traceable Computed Tomography*. PhD thesis, Technical University of Denmark, Kgs. Lyngby, 2013.

[15] Timm Weitkamp and Pierre Bleuet. Automatic geometrical calibration for x-ray microtomography based on Fourier and Radon analysis. In *Developments in X-Ray Tomography IV*, volume 5535, pages 623–627. International Society for Optics and Photonics, 2004.

[16] Elke Van de Casteele, Dirk Dyck, Jan Sijbers, and Erik Raman. A Model-Based Correction Method for Beam Hardening Artefacts in X-ray microtomography. *Journal of X-Ray Science and Technology*, 12(1):43–57, 2003.

[17] L. Alan Love and Robert A. Kruger. Scatter estimation for a digital radiographic system using convolution filtering. *Medical Physics*, 14(2):178–185, 1987.

[18] Miguel Sun and Josh M. Star-Lack. Improved scatter correction using adaptive scatter kernel superposition. *Physics in Medicine & Biology*, 55(22):6695–6720, 2010.

[19] Josh Star-Lack, Mingshan Sun, Anders Kaestner, Rene Hassanein, Gary Virshup, Timo Berkus, and Markus Oelhafen. Efficient scatter correction using asymmetric kernels. In Ehsan Samei and Jiang Hsieh, editors, *Medical Imaging 2009: Physics of Medical Imaging*, volume 7258, pages 644 – 655, 2009. Backup Publisher: International Society for Optics and Photonics.

[20] Navnina Bhatia, David Tisseur, Fanny Buyens, and Jean Michel Létang. Scattering correction using continuously thickness-adapted kernels. *NDT & E International*, 78:52–60, 2016. Publisher: Elsevier.

[21] Wim Van Aarle, Willem Jan Palenstijn, Jeroen Cant, Eline Janssens, Folkert Bleichrodt, Andrei Dabravolski, Jan De Beenhouwer, Kees Joost Batenburg, and Jan Sijbers. Fast and flexible X-ray tomography using the ASTRA toolbox. *Optics express*, 24(22):25129–25147, 2016. Publisher: Optical Society of America.

[22] Yi Sun, Ying Hou, Fengyong Zhao, and Jiasheng Hu. A calibration method for misaligned scanner geometry in cone-beam computed tomography. *NDT & E International*, 39(6):499–513, 2006.

[23] Jochen Hiller, Michael Maisl, and Leo Reindl. Physical characterization and performance evaluation of an x-ray micro-computed tomography system for dimensional metrology applications. *Measurement Science and Technology*, 23(8):085404, 2012.

[24] Michael Krumm, Stefan Kasperl, and Matthias Franz. Reducing non-linear artifacts of multi-material objects in industrial 3D computed tomography. *NDT & E International*, 41(4):242–251, 2008.

[25] Krishanan Arunmuthu, M. Ashish, Thangavelu Saravanan, John Philip, B. P. C. Rao, and T. Jayakumar. Simulation of beam hardening in X-ray tomography and its correction using linearisation and pre-filtering approaches. *Insight - Non-Destructive Testing and Condition Monitoring*, 55(10):540–547, 2013.

[26] Chalinee Thanasupsombat, Saowapak S. Thongvigitmanee, Sorapong Aootaphao, and Pairash Thajchayapong. A Simple Scatter Reduction Method in Cone-Beam Computed Tomography for Dental and Maxillofacial Applications Based on Monte Carlo Simulation. *BioMed Research International*, 2018:1–15, 2018.

[27] Ammar Alsaffar, Gasim Mammadov, and Sven Simon. Scattering Correction of CBCT Projections for the Quality Enhanced CT Reconstruction Using an Efficient Monte Carlo Photon Transport Model. In *10th Conference on Industrial Computed Tomography, Wels, Austria (iCT 2020)*, 2020.

[28] Steven W. Smith and Robert A. Kruger. A signal processing model of diagnostic x-ray scatter. *Medical physics*, 13(6):831–835, 1986. Publisher: Wiley Online Library.

[29] John M. Boone, Ben A. Arnold, and James Anthony Seibert. Characterization of the point spread function and modulation transfer function of scattered radiation using a digital imaging system. *Medical Physics*, 13(2):254–256, 1986.

[30] James Anthony Seibert and John M. Boone. X-ray scatter removal by deconvolution. *Medical Physics*, 15(4):567–575, 1988.

[31] Heng Li, Radhe Mohan, and Xiaorong Ronald Zhu. Scatter kernel estimation with an edge-spread function method for cone-beam computed tomography imaging. *Physics in Medicine & Biology*, 53(23):6729–6748, 2008.

[32] Bernd Ohnesorge, Thomas Flohr, and Klaus Klingenbeck-Regn. Efficient object scatter correction algorithm for third and fourth generation CT scanners. *European Radiology*, 9(3):563–569, 1999.

[33] Robin Degeilh. *Développement expérimental et modélisation d'un essai de fatigue avec gradient thermique de paroi pour application aube de turbine monocristalline.* PhD thesis, École normale supérieure de Cachan-ENS Cachan, 2013.

[34] Sandeep Patil and Bhallamudi Ravi. Voxel-based Representation, Display and Thickness Analysis of Intricate Shapes. In *Ninth International Conference on Computer Aided Design and Computer Graphics (CAD-CG'05)*, pages 415–422, Hong Kong, China, 2005. IEEE.